

Blood-retina barrier failure and vision loss in neuron-specific degeneration

Elena Ivanova, ... , Glen T. Prusky, Botir T. Sagdullaev

JCI Insight. 2019;4(8):e126747. <https://doi.org/10.1172/jci.insight.126747>.

Research Article

Ophthalmology

Vascular biology

Changes in neuronal activity alter blood flow to match energy demand with the supply of oxygen and nutrients. This functional hyperemia is maintained by interactions among neurons, vascular cells, and glia. However, how changing neuronal activity prevalent at the onset of neurodegenerative disease affects neurovascular elements is unclear. Here, in mice with photoreceptor degeneration, a model of neuron-specific dysfunction, we combined the assessment of visual function, neurovascular unit structure, and blood-retina barrier permeability. We found that the rod loss paralleled remodeling of the neurovascular unit, comprising photoreceptors, retinal pigment epithelium, and Muller glia. When substantial visual function was still present, blood flow became disrupted and the blood-retina barrier began to fail, facilitating cone loss and vision decline. Thus, in contrast to the established view, the vascular deficit in neuronal degeneration is not a late consequence of neuronal dysfunction but is present early in the course of disease. These findings further establish the importance of vascular deficit and blood-retina barrier function in neuron-specific loss and highlight it as a target for early therapeutic intervention.

Find the latest version:

<https://jci.me/126747/pdf>



Blood-retina barrier failure and vision loss in neuron-specific degeneration

Elena Ivanova, Nazia M. Alam, Glen T. Prusky, and Botir T. Sagdullaev

Burke Neurological Institute at the Weill Cornell Medicine, White Plains, New York, USA.

Changes in neuronal activity alter blood flow to match energy demand with the supply of oxygen and nutrients. This functional hyperemia is maintained by interactions among neurons, vascular cells, and glia. However, how changing neuronal activity prevalent at the onset of neurodegenerative disease affects neurovascular elements is unclear. Here, in mice with photoreceptor degeneration, a model of neuron-specific dysfunction, we combined the assessment of visual function, neurovascular unit structure, and blood-retina barrier permeability. We found that the rod loss paralleled remodeling of the neurovascular unit, comprising photoreceptors, retinal pigment epithelium, and Muller glia. When substantial visual function was still present, blood flow became disrupted and the blood-retina barrier began to fail, facilitating cone loss and vision decline. Thus, in contrast to the established view, the vascular deficit in neuronal degeneration is not a late consequence of neuronal dysfunction but is present early in the course of disease. These findings further establish the importance of vascular deficit and blood-retina barrier function in neuron-specific loss and highlight it as a target for early therapeutic intervention.

Introduction

Uninterrupted blood flow through an elaborate vascular network serves to match the high metabolic demands of the CNS with a supply of oxygen and nutrients. Direct exposure to blood, however, is fatal to neurons (1–5). Both vascular and neuronal diseases, such as stroke, diabetic neuropathy, Alzheimer's disease, and Huntington's disease, have been linked to disrupted neurovascular interactions and a failed blood-brain barrier (BBB; ref. 6). In neurodegenerative diseases, BBB disruption is commonly attributed to manifest stages of the disease. However, the dynamics of these changes during stages of disease when significant function is still present are less clear. As a part of the CNS, the retina serves as a tractable model to study these interactions. A neuron-specific perturbation is possible in the retina, because single mutations in photoreceptors result in a robust vascular phenotype in patients and in rodent models of retinal diseases. In addition, the visual function can be assessed noninvasively with light, and the structural integrity of the blood-retina barrier (BRB), a retina-specific BBB, can be determined with fluorescent probes.

In the retina, photoreceptors are normally shielded by 2 types of BRBs. The outer barrier comprises tight junctions of the retinal pigment epithelium (RPE), whereas the inner BRB is established by tight junctions of endothelial cells (Figure 1A). The inner BRB is similar to the canonical barrier of the CNS (7), and the outer barrier formed by the RPE is at the interface of the photoreceptors and choroid, a massive non-CNS vasculature. In retinal degenerative disease (RD), numerous single-gene mutations in rod photoreceptors not only lead to rod pathology, but are also harmful to their cellular neighbors (8–10). For example, cones, which are critical for everyday activities, such as discriminating colors, reading, driving, and recognizing faces, do not express defective rod proteins, but they degenerate after rods are lost (11–13). The secondary loss of cones in RD is the major cause of blindness and disability, and its cause is a subject of intense investigation. Messenger of this so-called “bystander” effect is thought to be a death signal released by degenerating rods that reaches cones through gap junctions (14). The absence of viability factors from rods may also compromise cone survival (15, 16). For example, changes in the rapamycin pathway have been shown to contribute to cone death (13). Whereas these studies have focused primarily on cone fate in the late stages of RD, there is growing evidence in both animal models (17, 18) and human patients (19) that rod dysfunction or their loss in the course of disease can affect cones through changes in neurovascular interactions. Targeting vascular pathology, even at the advanced stages of vision loss, has shown significant ability to improve photoreceptor survival and visual function (20).

Conflict of interest: GTP is the president of CerebralMechanics Inc., which manufactures the virtual optokinetic system used in the study.

Copyright: © 2019 American Society for Clinical Investigation

Submitted: December 11, 2018

Accepted: March 14, 2019

Published: April 18, 2019.

Reference information: *JCI Insight*. 2019;4(8):e126747. <https://doi.org/10.1172/jci.insight.126747>.

The purpose of this study was to dissect the dynamics of these changes at the stages of RD when visual function was still preserved. We combined the assessments of cone-mediated visual function, neurovascular unit structure, and the BRB permeability in *rd10* mice, an established model of slow photoreceptor degeneration. Since adequate blood supply and BBB integrity are critical to neuronal survival and function, these findings expand our understanding of neuronal degeneration and should help inform the development of safe and effective therapies.

Results

Timeline of visually driven behavior decline and BRB failure. Since the decline of cone vision represents the most devastating phase of RD, we compared cone-mediated visual function in WT and *rd10* mice, an established RD model with rod photoreceptor-specific deficiency (21). Young *rd10* mice had spatial frequency (acuity) responses that were comparable to those of WT mice up to P31 (Figure 2, A and B; WT = 0.39 ± 0.02 , $n = 13$ mice; *rd10* = 0.36 ± 0.03 , $n = 20$ mice), which gradually declined thereafter. Whereas some animals were unresponsive as early as P75, many animals had low, but measurable, vision as late as P160. This is contrary to the assumption based on ERG recordings that the strain would be blind (9, 22). These responses were not driven by melanopsin intrinsically photosensitive retinal ganglion cells, since visually driven behavior of *rd10* mice was in contrast to no light-driven responses of melanopsin-only mice (*Gnat1^{-/-}/Cnga3^{-/-}/Opn4^{+/+}* mice; ref. 23) and mice lacking rod, cone, and melanopsin photoreception (*Gnat1^{-/-}/Cnga3^{-/-}/Opn4^{-/-}* mice; ref. 23).

The eyes of WT mice did not exhibit high variability, neither between different animals nor between the eyes of the same mouse (Figure 2B). In contrast, there was significant variability between the 2 eyes of the same *rd10* animal (Figure 2C, both eyes of the same animal tested) and across individual mice ($P = 0.019$; $n = 20$ mice, ANOVA). We hypothesized that variability in *rd10* was driven by local factors contributing to the progression of cone dysfunction. In neurodegenerative diseases, changes in blood flow and BBB breakdown have been associated with neuronal dysfunction and cell death. However, despite association between rod degeneration and BRB failure (18), vascular dysfunction has not been considered as an early factor in RD. We next tested the integrity of BRB at 2 time points: shortly after rod degeneration and at an advanced stage of the RD. Mice were intravenously injected with 3- to 5-kDa fluorescent dextran, and the retina was imaged *in vivo* under confocal microscope (Figure 2D). At P35–P40, in contrast to WT mice, in which the primary retinal veins and arteries were prominent, the *rd10* vessels were significantly constricted (WT: arteries, diameter [d] = 36.1 ± 4.0 μm , veins d = 44.9 ± 6.9 μm , capillaries d = 8.5 ± 0.8 μm ; *rd10*: arteries d = 27.9 ± 3.2 μm , $P = 0.0007$, veins d = 34.2 ± 4.7 μm , $P = 0.003$, capillaries d = 9.3 ± 1.2 μm $P = 0.14$, ANOVA; $n = 4$ mice in each group). Importantly, blood vessel constriction was paralleled by reduction in blood flow (Figure 2, E–G). Since both WT and *rd10* mice used in the current study share a C57BL6J genetic background, which has not been reported to develop variable or abnormal intraocular blood pressure (24), we attributed the blood flow reduction to vascular constriction. Constriction of the primary blood vessels in RD was also evident at P200 (WT: arteries d = 36.2 ± 6.3 μm , veins d = 45.9 ± 7.9 μm , capillaries d = 8.8 ± 0.9 μm ; *rd10*: arteries d = 27.7 ± 4.4 μm , $P = 0.005$, veins d = 32.2 ± 2.9 μm , $P = 0.001$, capillaries d = 9.1 ± 1.0 μm , $P = 0.5$, ANOVA; $n = 4$ mice in each group). In addition to general narrowing, the primary arteries exhibited periodic constrictions, “beading” along their length (Figure 2D, arrows, and Figure 2F, wavy red dashed line). When multiple diameter measurements were taken along those blood vessels (25) the variability of measurements was larger in *rd10* arteries (Figure 2F, top, P40: WT SD = 1.79, 4 mice; *rd10* SD = 3.1, 4 mice; P200: WT SD = 2.1, 3 mice; *rd10* SD = 4.8, 4 mice). Due to optical limitations imposed by a mouse lens (26), the constriction of the capillaries in the superficial layer of *rd10* mice was not reliably measured *in vivo* and was further assessed in eyecup explants (see below).

In WT mice, no fluorescence was detected outside of the retinal blood vessels in any vascular layer at any age, confirming the integrity of the BRB (Figure 2, D and H). At P40 in *rd10* retina, however, a diffuse fluorescence was visible outside of blood vessels and adjacent to the RPE (WT deep layer normalized intensity [I_{norm}] = 3.41 ± 1.41 , *rd10* deep layer, I_{norm} = 9.01 ± 3.37 , $P = 0.04$; WT RPE I_{norm} = 2.73 ± 0.90 , *rd10* RPE, I_{norm} = 12.95 ± 4.21 , $P = 0.007$, ANOVA; $n = 5$ mice). In P200 *rd10* mice, vascular leak was present not only near RPE, but also around capillaries in the deep vascular layer (WT deep layer I_{norm} = 3.02 ± 0.69 , *rd10* deep layer, I_{norm} = 13.18 ± 2.88 , $P = 0.0002$; WT RPE I_{norm} = 2.20 ± 0.45 , *rd10* RPE, I_{norm} = 30.07 ± 12.34 , $P = 0.0003$, ANOVA; $n = 5$ mice). Thus, a perfusion deficit and a progressive breakdown of the outer and inner BRBs coincided with the onset of cone dysfunction in RD.

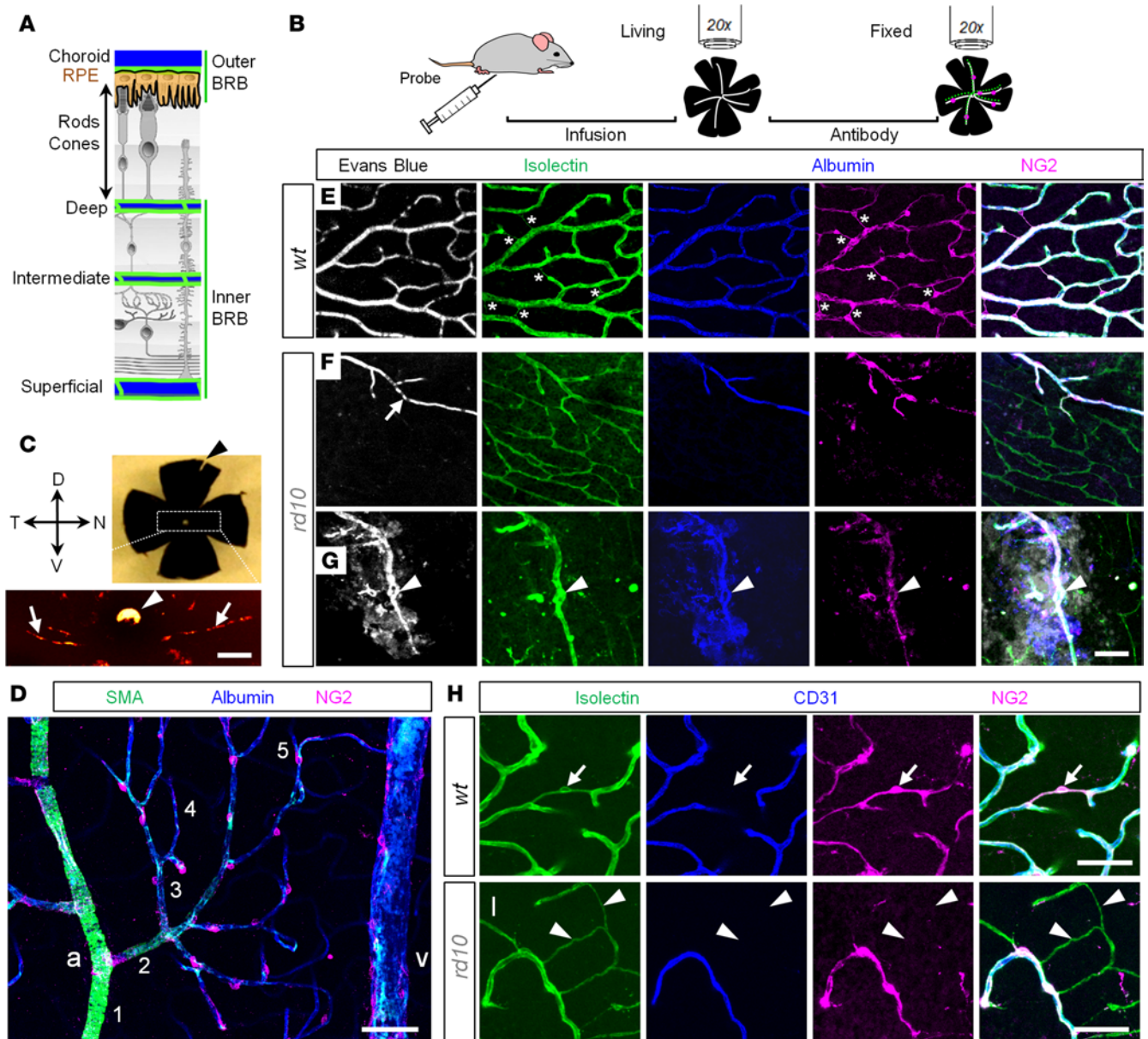


Figure 1. Combinatorial approach for assessment of the vascular network and blood-retina barrier in living and fixed retinal tissue. (A) A dual nature of blood supply in the retina. Photoreceptors and retinal pigment epithelium (RPE) separate the outer and inner blood-retina barriers (BRBs). (B) BRB assessment protocol. (C) Identification of retinal poles in the eyecup preparation. The nasal-temporal axis is aligned with light choroidal marks (arrows); the dorsal pole corresponds to the white spot of the optic nerve head (arrowhead). (D) Hierarchy of retinal blood vessels. a, artery; v, vein. Numbers indicate branch order. (E–G) Quadruple-labeled confocal sections of the deep vascular layer in WT (E) and *rd10* mice at P200 (F and G). A structural marker, isolectin, revealed a net of blood vessels in WT and *rd10* retinas (green). In WT retina, all vessels were perfused by Evans Blue (white). In *rd10* retina, only a fraction of capillaries was functional (F, arrow). Tortuous blood vessels in *rd10* retina were leaky (G, arrowheads). In the fixed tissue, albumin (blue) reproduced Evans Blue pattern. Pericytes, labeled for neuron-glia antigen 2 (NG2), concentrated on perfusable blood vessels (magenta; bridging pericytes are marked by asterisks). In merged images, images were aligned by warp procedure to compensate for fixation-related distortion. (H and I) Isolectin (green) labels basement membrane around pericytes (magenta) and endothelial cells (blue); a bridging pericyte is shown (arrows). Degenerating retinal blood vessels in *rd10* retina form empty vascular sleeves without endothelial cells or pericytes (I, arrowheads). Scale bars: 250 μm (C), 50 μm (D–I). SMA, smooth muscle actin; CD31, cluster of differentiation 31.

Failure of the RPE barrier precedes disruption of the inner BRB. To establish the dynamics of BRB failure in RD, we used fluorescent probes of increasing size injected in living mice (Figure 3A). To account for the possibility of long-term leakage, we also evaluated the accumulation of the blood albumin amplified with an antibody. Mice were sacrificed 30 minutes following probe infusion. Freshly isolated eyecups with lens removed were analyzed with confocal microscopy; the images were taken from the central retina. The

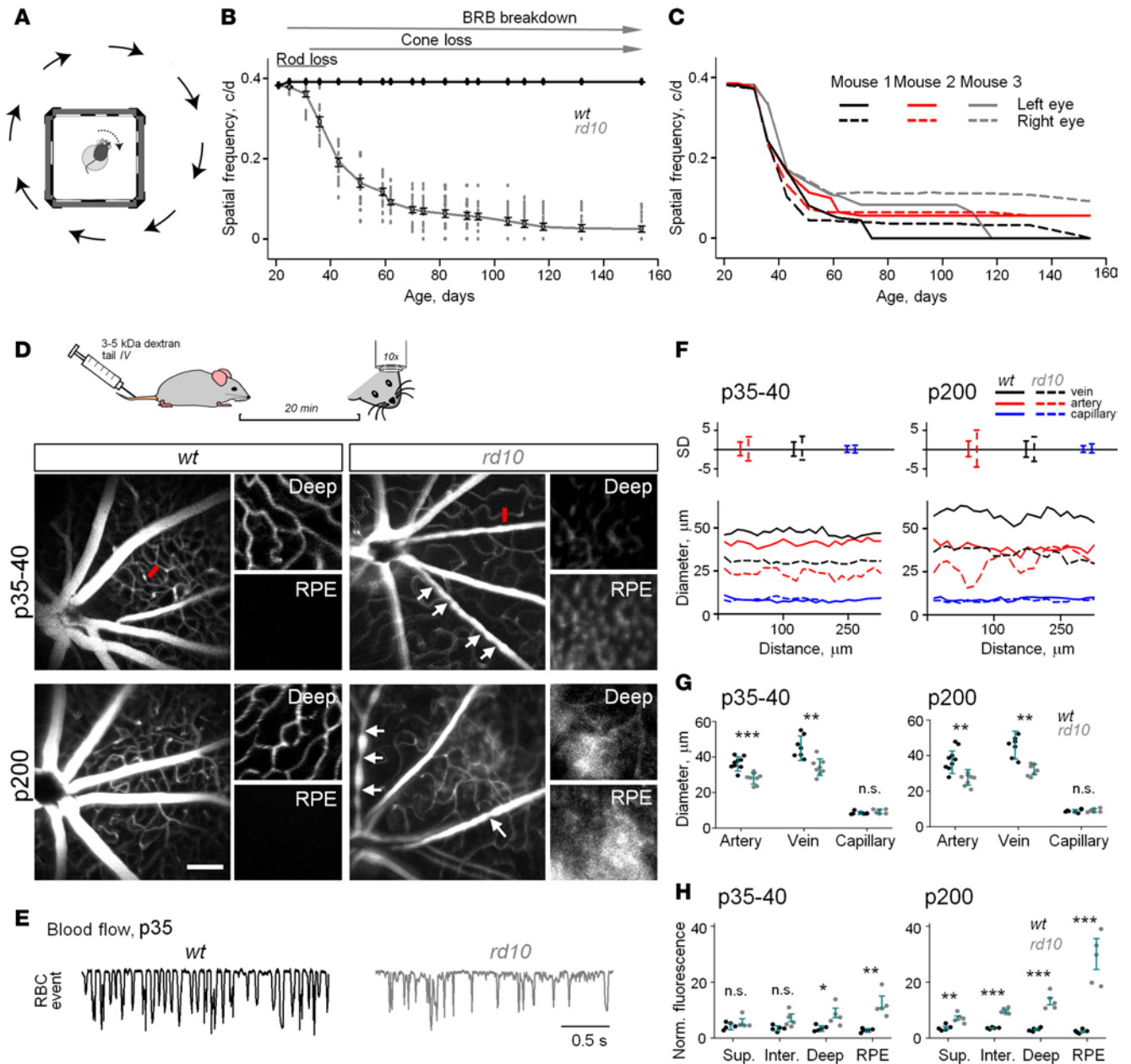


Figure 2. Cone function decline, the onset of vascular changes, and blood-retina barrier and blood flow disruption in retinal degeneration. (A) Behavior assessment of mouse vision. **(B)** Cone-mediated behavior persisted in *rd10* mice until P160. The same animals (13 WT and 20 *rd10*, ANOVA) were measured in a longitudinal manner (both eyes of the same mouse were measured separately at each time point; only one eye's measures were plotted in the figure). **(C)** Longitudinal analysis of variations between 2 eyes in a given *rd10* mouse shows that extent of the vision decline varied across the 2 eyes of the same animal (3 different *rd10* mice, 2-tailed *t* test). **(D)** In vivo confocal assessment revealed constricted vasculature and compromised blood-retina barrier (BRB) in RD. Small images are magnified areas of retinal pigment epithelium (RPE) and the deep retinal vascular layers. **(E)** Rate of capillary retina blood cell (RBC) flow at P35, measured as a number of cells crossing a red line in **D**. Each cell crossing is represented by a deflection and is reduced in *rd10* mice at P35. **(F)** Comparison of diameters from images in **D**, showed narrowing (bottom) and uneven constriction of blood vessels, as measured by SD from means (top) in RD (arrows in **D**). **(G)** Averaged vascular diameter was significantly smaller in *rd10* mice Error bars \pm SD (4–5 mice, 2-tailed *t* test). **(H)** Vascular leak progressively increased in RD in the RPE and deep vascular layers (4–5 mice, 2-tailed *t* test). Scale bars: 100 μ m (**D**); 25 μ m (**E**). Error bars \pm SD (4–5 mice). **P* < 0.05, ***P* < 0.01, ****P* < 0.001.

eyecup preparation enabled a robust assessment of the retinal capillary network, RPE, and choroid. Similar to in vivo experiments, no leakage was detected in WT mice from P20 to P200 (Figure 3, B–E; P20, albumin, deep layer $I_{norm} = 0.14 \pm 0.02$; RPE $I_{norm} = 0.09 \pm 0.02$; P20, fluorescein, deep layer $I_{norm} = 0.07 \pm 0.01$; RPE $I_{norm} = 0.01 \pm 0.01$; P40, albumin, deep layer $I_{norm} = 0.24 \pm 0.03$; RPE $I_{norm} = 0.19 \pm 0.02$; P40, fluorescein, deep layer $I_{norm} = 0.04 \pm 0.01$; RPE $I_{norm} = 0.01 \pm 0.01$; P200, albumin, deep layer $I_{norm} = 0.08$

± 0.02 ; RPE $I_{\text{norm}} = 0.05 \pm 0.01$; P200, fluorescein, deep layer $I_{\text{norm}} = 0.05 \pm 0.01$; RPE $I_{\text{norm}} = 0.05 \pm 0.01$; $n = 4-5$ mice in each group). In *rd10* retinas, the first appearance of leakage, which outlined the borders of RPE cells (Figure 3B, top), was detected as early as P20–P21 with the 0.4-kDa fluorescein, the smallest size used (P20, albumin, deep layer $I_{\text{norm}} = 0.18 \pm 0.04$; RPE $I_{\text{norm}} = 0.13 \pm 0.05$; P20 fluorescein, deep layer $I_{\text{norm}} = 0.10 \pm 0.02$; RPE $I_{\text{norm}} = 0.11 \pm 0.01$). The leak did not diffuse to the deep vascular layer, separated from the RPE by multiple rows of photoreceptors. At P35–P40, a more pronounced leak was determined by fluorescein and 2- to 4-kDa dextran around RPE of *rd10* mice (P40, fluorescein, deep layer $I_{\text{norm}} = 0.26 \pm 0.05$, $P = 0.0029$; RPE $I_{\text{norm}} = 0.35 \pm 0.06$, $P = 0.0003$, ANOVA; $n = 5$ mice). In the central retina of the P35–P40 *rd10* mouse, the majority of rods have degenerated, leaving only a row of cones between the deep vascular layer and the RPE. Therefore, the leak from RPE cells, seen in Figure 2D and Figure 3B, is likely to spread into the nearby deep layer. With the increasing probe size, leakage diminished and was almost undetectable with 70-kDa Evans Blue (Figure 3, C–G). Accumulation of plasma albumin (70 kDa), however, was already evident at P35 (albumin, deep layer $I_{\text{norm}} = 0.43 \pm 0.02$, $P < 0.001$; RPE $I_{\text{norm}} = 0.52 \pm 0.02$, $P < 0.001$, ANOVA; $n = 5$ mice), suggesting chronic accumulation. Whereas no leakage from retinal capillaries was detected in the deep layer of *rd10* mice at P35–P40, all capillaries were constricted. At P200, an increased leak near the RPE was detected with all probes, suggesting progressive decline of the outer BRB. In addition, evidence of leakage was present around tortuous dilated capillaries in the deep vascular layer. Thus, after rod death, vascular leakage develops first at the outer BRB and then later at the inner BRB, which could alter the extracellular environment and expose neurons to blood.

Cone degeneration parallels the vascular leakage. To determine whether reduced integrity of the BRB affected cone survival, we correlated cone morphology and survival with BRB integrity. In WT retina, the highest density of cones is in the central retina (27). At P35 *rd10*, cone loss was evident across all eccentricities, with the highest drop in the central region (Figure 4A). Compromised BRB was also evident in the central retina (Figure 4, A and G). Consistently, at the same retinal eccentricity, we found negative correlation between presence of cones and plasmalemma vesicle-associated protein (PLVAP)/albumin leakage (Figure 4, B–E). Indeed, the Mander's indices showed that there was little to no overlap between the areas with cones and the regions with leak (Figure 4, F and G).

At P200, we found surviving cones concentrated around the dorsal pole of the retina in midperipheral and peripheral regions (Figure 5, green; $P = 0.002$ for central retina, $P < 0.001$ for peripheral retina). The regions with leaky blood vessels lacked cones (Figure 5D). The distribution of surviving cones was skewed to the regions without albumin and PLVAP, a fenestration marker undetected in the WT retinal preparations (28). The patchy cone distribution in the advanced RD had a strong negative correlation with the presence of compromised BRB, as reflected by low Mander's indices (Figure 5, F and G). Cone survival was higher in the peripheral areas where fewer leaks were detected.

Disruption of BRB is not driven by pericyte loss. Next, we investigated the factors contributing to the disruption of the BRB in RD. In diabetic retinopathy (29, 30) and other vascular pathologies of the CNS, compromised blood barrier and vascular leakage have been associated with the loss of pericytes (31). We tested whether leaky retinal blood vessels in RD were also linked to pericyte loss. Two kinds of pathological capillaries were detected in RD: degenerating nonperfusable capillaries (Figure 6, A–F) and dilated tortuous capillaries (Figure 6G). The density of perfused blood vessels was significantly higher in WT mice at both P35–P40 (Figure 6E WT, $d = 15.9 \pm 0.4 \text{ mm}/0.4 \text{ mm}^2$; *rd10*, $d = 6.8 \pm 0.8 \text{ mm}/0.4 \text{ mm}^2$; $P < 0.001$, $n = 5$ mice in each group) and P200 (Figure 6F, WT, $d = 11.70.4 \text{ mm}/0.4 \text{ mm}^2$; *rd10*, $d = 1.1 \pm 0.2 \text{ mm}/0.4 \text{ mm}^2$; $P < 0.001$, ANOVA; $n = 5$ mice in each group). Unexpectedly, in *rd10* mice we found a number of surviving pericytes that were not directly located on the functional blood vessels (Figure 6, B–D, arrowheads). In fact, these pericytes were located on fully constricted nonperfusable blood vessels. This suggests that a point of contact between a pericyte branch and functional blood vessel is sufficient to support pericyte survival. This observation is consistent with the elevated ratio of pericytes to albumin-positive blood vessels in *rd10* mice (Figure 6, E and F). As RD progressed, a distinct type of retinal capillary had emerged exclusively in the deep vascular layer (Figure 6G). These capillaries were tortuous and leaky. The pericytes around leaky capillaries survived, although their shape was distinct from those of unaffected regions. The persistence of pericytes around leaky capillaries suggests a distinct mechanism of vascular leakage in photoreceptor degeneration.

Leak of retinal blood vessels is triggered by displaced RPE cells. Since pericytes did not appear to be associated with vascular leak in RD, we analyzed other structural elements adjacent to degenerating photoreceptors: RPE, Muller glia, and choroid. To evaluate the integrity of BRB, eyecups were labeled for PLVAP (a fenestration

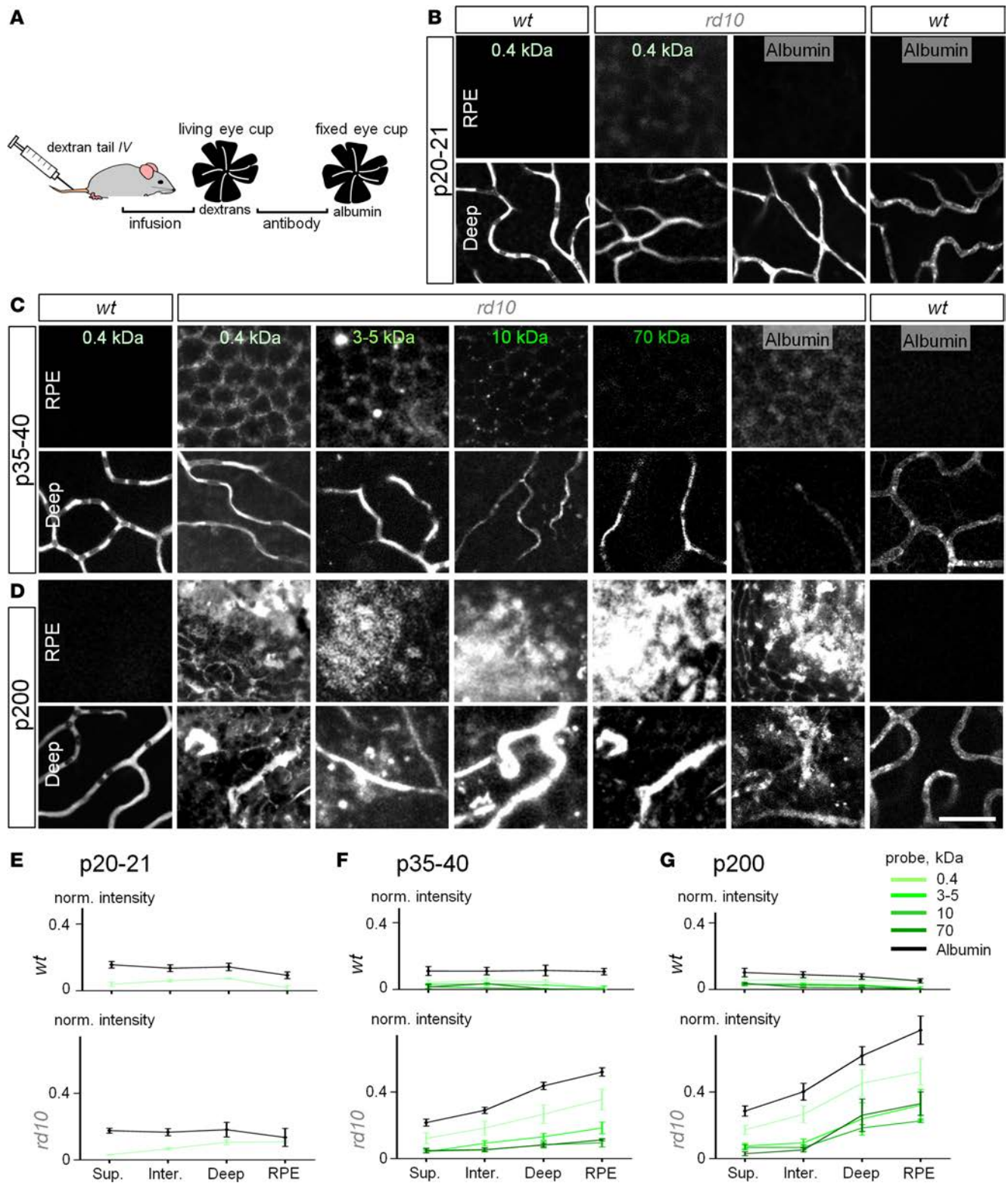


Figure 3. Blood-retina barrier is first disrupted at retinal pigment epithelium and later at retinal vasculature. (A) Mice were injected with fluorescent probes, and living eyecup preparations were imaged under confocal microscope and then processed for albumin labeling. (B) Representative images of WT and *rd10* retinas after infusion of probes. At P20–P21 light fluorescein labeling was detected at the retinal pigment epithelium (RPE) layer in *rd10* retina. In WT retina, both lowest weight fluorescein and highest weight accumulated albumin were contained to blood vessels. (C) At P35 in *rd10* retina, outer blood-retina barrier (BRB) had increased permeation for both low-weight-molecular probes and large (70-kDa) blood plasma albumin. (D) At P200 in *rd10* retina the leak was evident with all probes from both RPE and deep vascular capillaries. Scale bar: 50 μ m. (E–G) Quantification of the vascular leak at P20–P21 (E), P35–P40 (F), and P200 (G). Error bars \pm SEM. Each measurement was done in 4–5 different mice.

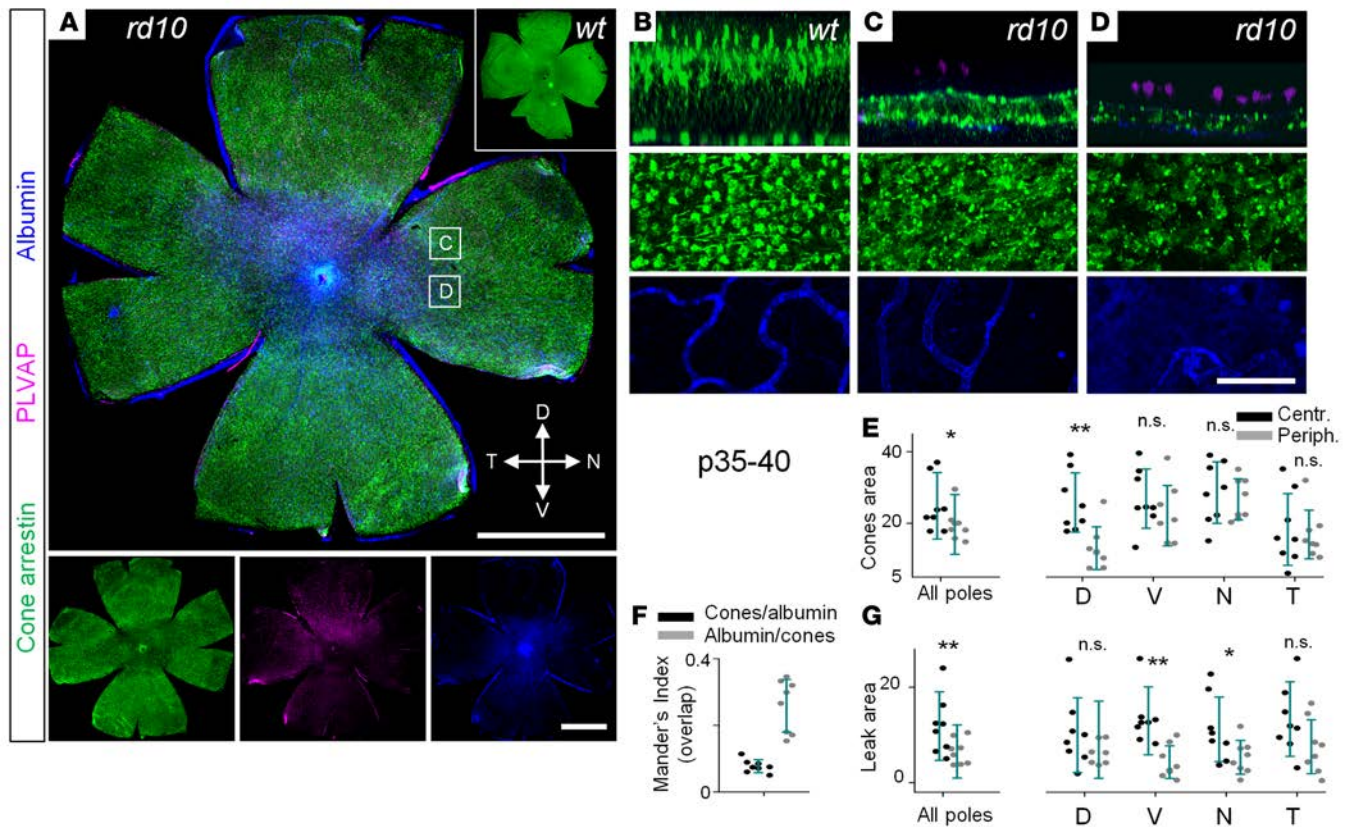


Figure 4. Topographic distributions of cones and blood-retina barrier failure following loss of rods. (A) In *rd10* mice, at P35–P40, cone densities (arrestin, green) were lower in the areas with vascular leak (albumin, blue). (B–D) Magnified areas from A. In WT mice, cones were evenly distributed through the retina; no albumin labeling was detected outside of the capillaries (B). In *rd10* mice, regions with leak and degenerating deep layer capillaries corresponded to lower densities of cones. (E) Quantification of cone-occupied areas across retinal poles. (F) Mander's indices show that areas with surviving cones and leaky areas do not overlap. (G) Leak was determined predominantly in the central areas at the level of retinal pigment epithelium. Scale bar: 1 mm (A); 50 μ m (B–D). Data are represented as average \pm SD (8 mice, each measurement). Two-tailed *t* test, **P* < 0.05, ***P* < 0.01. PLVAP, plasmalemma vesicle-associated protein.

marker normally expressed in choroidal capillaries and not found in retinal blood vessels) and claudin5, a tight junction component in the brain and retina (32). In the WT mice, all retinal blood vessels expressed claudin5 and were negative for PLVAP (Figure 7A). In *rd10* mice, however, numerous retinal blood vessels were positive for PLVAP and were leaky (Figure 7B, arrows). The PLVAP labeling on retinal capillaries colocalized with displaced RPE cells distinguished by labeling for phalloidin (an F-actin marker that binds to RPE cells; Figure 7, C and D) and by the presence of black melanin (Figure 7, E–K, pigmented cells). The shape of the displaced RPE was distorted from the characteristic honeycomb arrangement (compare WT, Figure 7C, and *rd10*, Figure 7D, arrowheads). In these areas, the expression of claudin5 was diminished (Figure 7, J and K, arrow) and albumin was present. We did not observe leaky PLVAP-positive blood vessels without RPE cells surrounding them. In contrast, we consistently found parts of the vasculature surrounded by RPE cells with no or very little PLVAP expression and vascular leak. It thus appears that RPE cells first contact the vasculature and then modify it. RPE cell displacement and migration along retinal blood vessels has also been documented in a different RD mouse model (rhodopsin^{-/-} mouse; ref. 33) and human patients (34). In contrast, blood vessels that were not in direct contact with RPE maintained their claudin5 labeling, were not leaky, and did not express PLVAP (Figure 7, E–K, arrowheads). The percentage of the PLVAP-positive retinal blood vessels was higher at the periphery (Figure 7L). The lower density of PLVAP-positive blood vessels at the dorsal pole was caused by the lowest density of the surviving retinal blood vessels (dorsal $d = 0.69 \pm 0.33$ mm/mm², ventral $d = 1.85 \pm 0.85$ mm/mm², nasal $d = 1.76 \pm 0.59$ mm/mm², temporal $d = 1.49 \pm 0.30$ mm/mm², $n = 5$ mice).

In the absence of RPE, the Muller glia seals leaky choroid. In addition to leaky retinal blood vessels, a different pathology of BRB emerged in the central retina of *rd10* mice (Figure 7B, arrowheads, and Figure 8U). In high-magnification images from those areas, choroidal capillaries become visible (Figure 8, M, P, and S). The

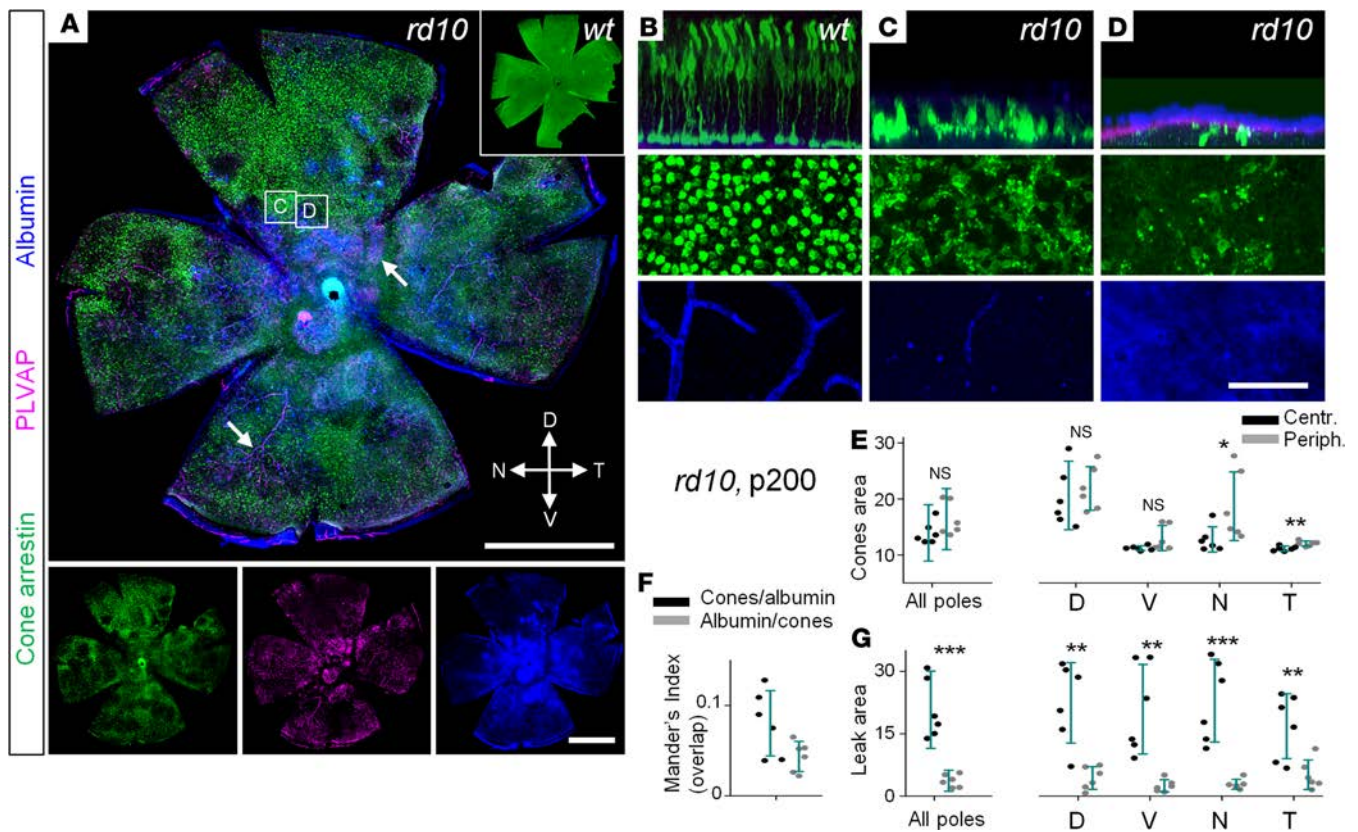


Figure 5. Cone loss and the presence of vascular leak in the advanced stages of retinal degeneration. (A) In *rd10* mice, cones (arrestin, green) were absent in the areas with vascular leak (albumin, blue) coming from fenestrated vasculature (plasmalemma vesicle-associated protein [PLVAP], magenta, arrows). (B–D) Magnified areas from A. In WT, cones were evenly distributed through the retina; no albumin labeling was detected outside of the capillaries. In *rd10* mice, regions with leak (D) corresponded to lower densities of cones. Most capillaries of the deep layer were degenerated in *rd10* mice. (E) The majority of the surviving cones were found in the periphery, especially of the dorsal pole. (F) Mander's indices show that areas with surviving cones and areas with blood-retina barrier leak do not overlap. (G) Leak was seen in patches, predominantly across central areas and around deep layer capillaries in the periphery. Scale bar: 1 mm (A); 50 μ m (B–D). Data are represented as average \pm SD (6 mice, each measurement). Two-tailed *t* test, **P* < 0.05, ***P* < 0.01, ****P* < 0.001.

choroidal capillaries were not visible in eyecup preparation from WT pigmented mice with intact RPE cells (Figure 8, A–C). When black-pigmented RPE cells were removed by a brush, PLVAP and albumin labeling became visible in choroidal capillaries (Figure 8, D–F); only large blood vessels outside of the choroidal capillary layer were labeled for claudin5 (Figure 8, arrow; those vessels were negative for PLVAP). In albino animals that naturally lack pigmentation, the labeling was identical to that of pigmented mice after RPE removal (Figure 8, G–I). Thus, in WT mice, choroidal capillaries, labeled for PLVAP, were normally masked by black nontransparent RPE cells and did not coexpress claudin5. In *rd10* mice, RPE cells were absent in patches where PLVAP-positive choroid became visible (Figure 8, J–T). Similar to WT mice, at the early stages of RD, exposed choroid did not express claudin5 (Figure 8, J–L). However, at the later stages, these bare choroid patches, marked by the absence of connexin43 (Figure 8, P and S), exhibited atypical expression of claudin5 (Figure 8N), and were adjacent to the Muller glia (Figure 8, S and T). Our data and data from other laboratories (35) demonstrate that, in the absence of RPE cells, Muller cell processes create a seal at Bruch's membrane. Moreover, in patients with geographic atrophy, some Muller cell processes penetrate the Bruch's membrane and, therefore, could contact choroidal capillaries (35). Interestingly, it was previously shown in rat eye that Muller glia, injected into the anterior chamber, induced barrier properties in the non-CNS vasculature of iris (36). Thus, our data provide further evidence for the potential of Muller glia to induce claudin5 expression and to repair BRB.

Discussion

In neuronal forms of RD, research and repair efforts have been focused on photoreceptor cells; the changes to other members of the neurovascular unit were interpreted as secondary and considered manifest at the advanced stages. Here, however, we show that (a) changes in the neurovascular elements surrounding pho-

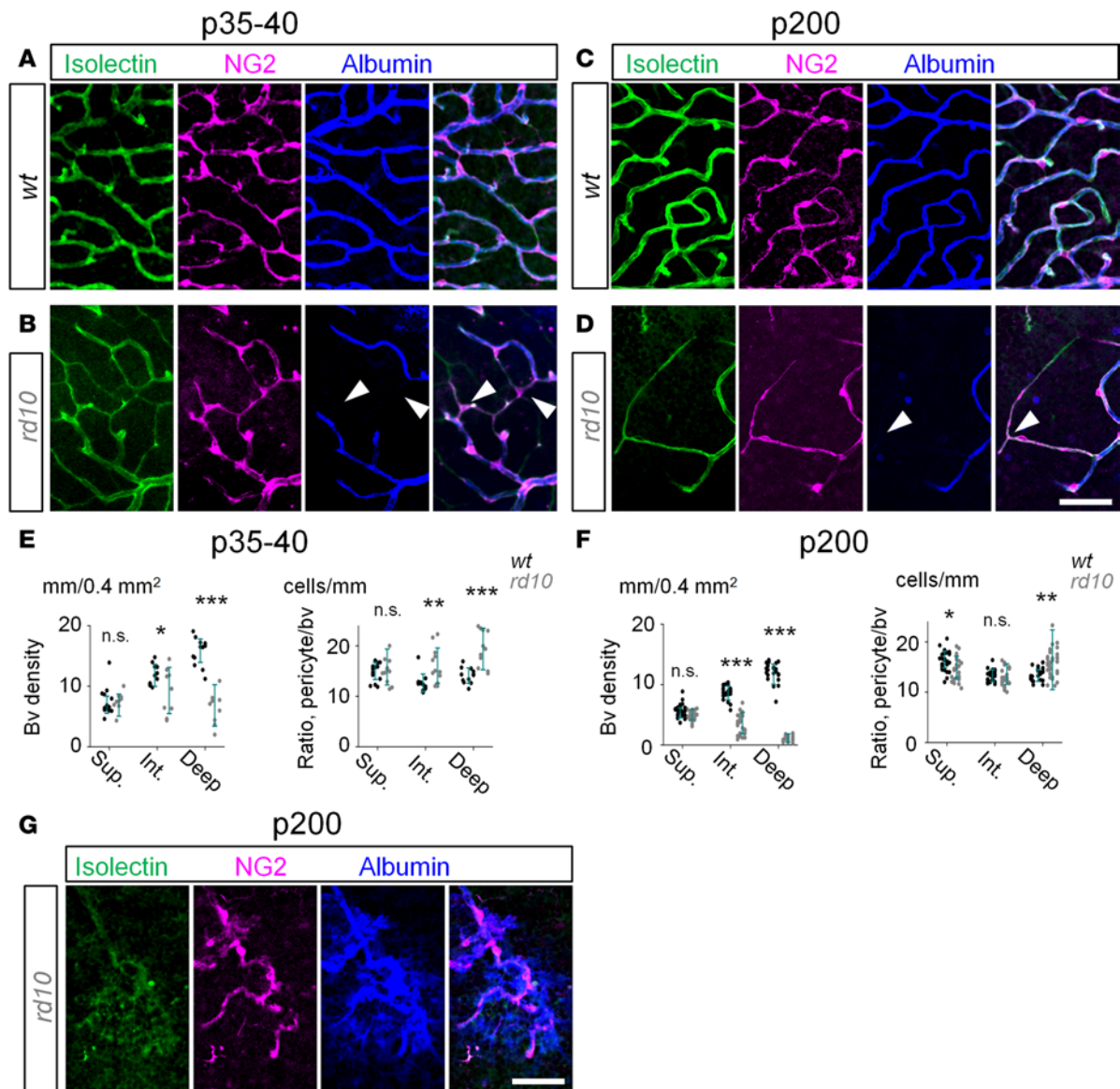
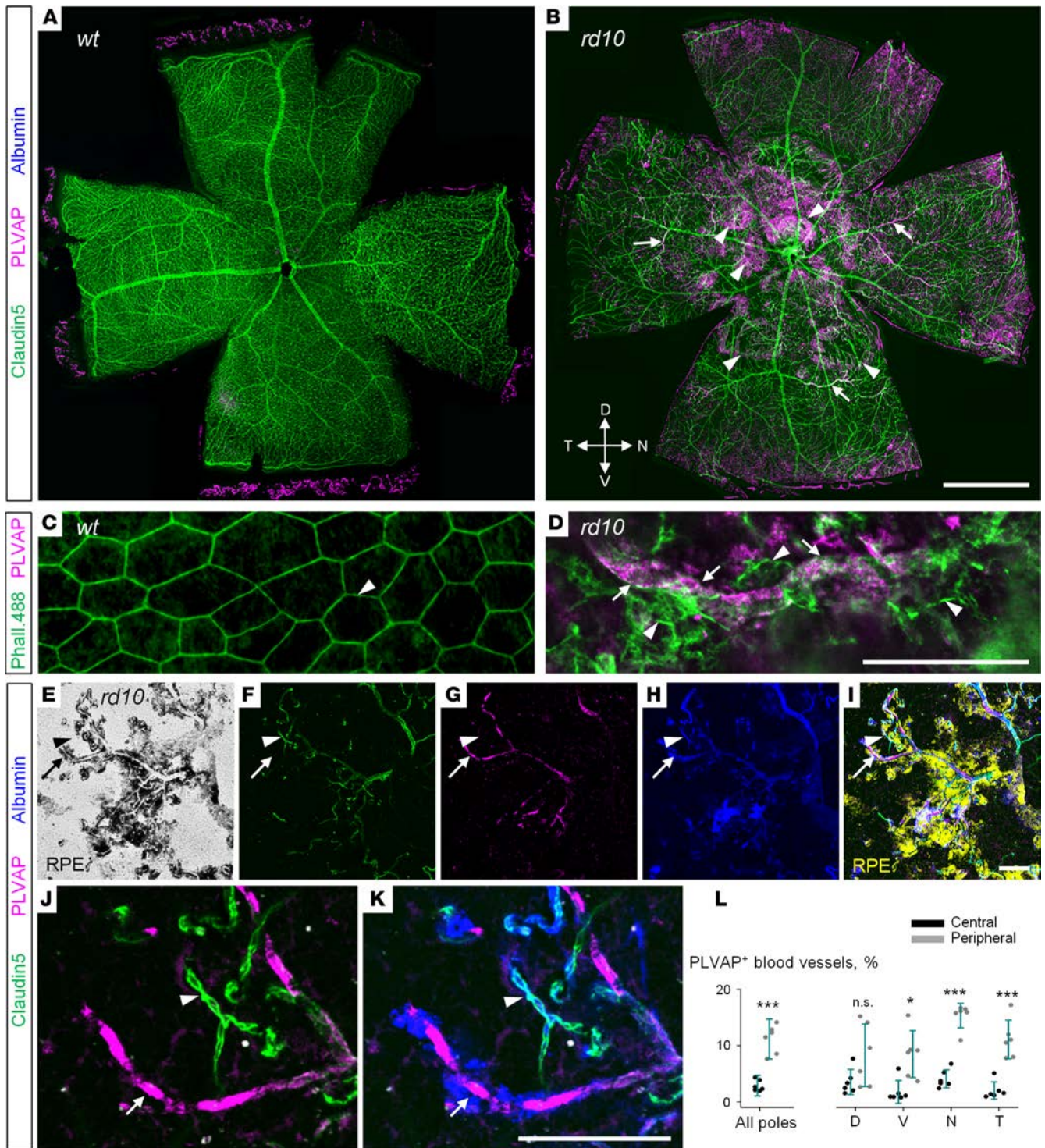


Figure 6. Disruption of blood-retina barrier in RD is not driven by the loss of pericytes. (A) In WT mice at P35–P40, all capillaries (green) were perfused, as revealed by albumin labeling (blue) and covered by pericytes (magenta). (B) In *rd10* mice, degenerating capillaries in the deep and intermediate layers were nonperfusable but contained pericytes (arrowheads). (C and D) At P200, capillaries were well perfused in WT mice while constricted in *rd10* mice. (E and F) In *rd10* mice, despite vascular decline, the ratio of pericyte to perfused capillaries increased due to persistence of pericyte on degenerated capillaries. (G) Tortuous leaky capillaries in the deep layer in *rd10* mice. Scale bar: 50 μ m. Average \pm SD (4–5 mice). Two-tailed *t* test, **P* < 0.05, ***P* < 0.01, ****P* < 0.001. NG2, neuron-glia antigen 2; bv, blood vessels.

toreceptors occurred at the stages of RD when substantial visual function was still present; (b) following the onset of rod degeneration, both inner and outer BRBs became progressively leaky; (c) retinal inner BRB was compromised by displaced RPE cells, (d) the Muller glia only partially “sealed” the choroid by inducing atypical expression of the tight junction component claudin5; and (e) cone loss and visual function decline were associated with the presence and severity of the BRB leak. Since BRB integrity is critical to neuronal function and survival, these findings expand our understanding of RD and should help inform the development of safe and effective vision repair therapies. Below, we discuss how degradation of neurovascular interactions, often inseparable neural and vascular changes, is integral to impairment in neurological disease.

Early changes in the BRB and vision loss. Despite their diversity, the majority of RDs are caused by various single gene mutations, resulting in the absence or expression of defective proteins in rod photoreceptors (Figure 9A, asterisk). Dysfunction and death of rods leads to night blindness, the first symptom of RD, but it is the death of cones that is responsible for the progressive loss of pattern vision and eventual blindness. In humans



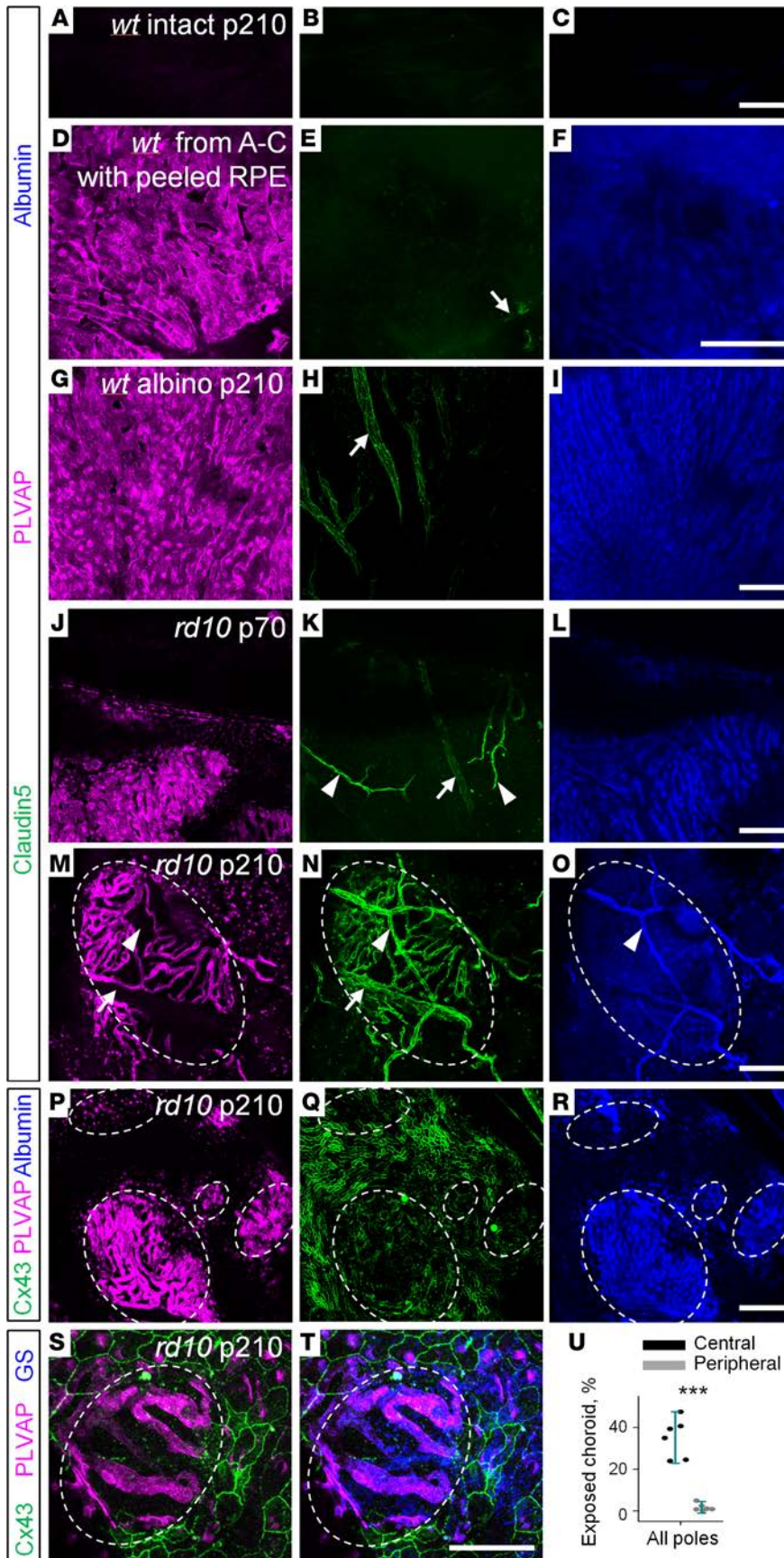


Figure 8. Emergence of blood-retina barrier elements in choroid where retinal pigment epithelium is compromised. (A-C) In WT eyecup preparation, stained for claudin5, PLVAP, and albumin, no labeling is visible through pigmented retinal pigment epithelium (RPE) cells. (D-F) In pigmented mice from A-C, RPE cells were removed after the eyecup preparation was imaged. (D-I) In WT pigmented and albino mice, choroid capillaries expressed PLVAP (magenta) and did not express claudin5 (green). In contrast, large, sparse, deeply positioned choroid blood vessels were positive for claudin5 and negative for PLVAP (arrow). (J-L) In *rd10* mice at P70, exposed capillaries of choroid had no claudin5 expression. Due to the absence of photoreceptors, retinal blood vessels became visible (arrowheads). The arrow shows large choroid blood vessels behind choroid capillary layer. (M-O) At P210 in *rd10*, choroid gained claudin5 expression in the bare patches without RPE cells (circled). (P-R) In the absence of RPE labeled for Cx43 (green), choroid became exposed and leaky (blue). (S and T) Muller glia, immunostained for glutamine synthetase (GS, blue), were associated with the exposed choroid (outlined by the dashed line). (U) Exposed choroid was mostly present in the central retina. Scale bars: 0.1 μ m. Average \pm SD (6 mice). Two-tailed *t* test, ****P* < 0.001. PLVAP, plasmalemma vesicle-associated protein; alb, albumin; Cx43, connexin43.

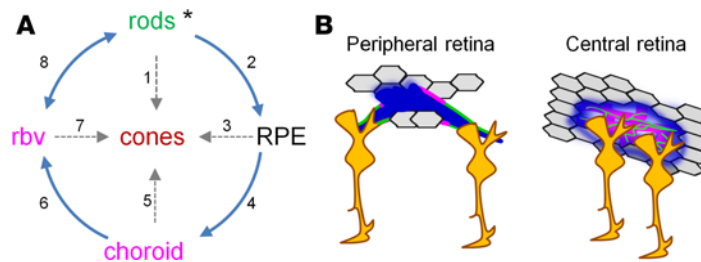


Figure 9. Multiple pathways leading to cone death in RD. (A) Primary and secondary pathways affecting cone survival. For individual pathways refer to the Discussion. (B) Mechanisms of the inner BRB (left) and outer BRB (right) breakdown in retinal degeneration. In the periphery, RPE cells get in contact with retinal blood vessels and release factors, such as VEGF, to induce fenestration of retinal capillaries. At the same time, diminished contact with Müller glia causes decreased expression of tight junction protein claudin5. In the central retina, inside the patches of lost RPE cells, the choroid become leaky. Müller glia attracted by exposed choroid and blood create a glial seal by atypical expression of tight junction proteins in choroid. BRB, blood-retina barrier; RPE, retinal pigment epithelium; rbv, retinal blood vessels.

(37) and rodents (Figure 2B), cone function contributes to visually driven behavior, until advanced stages of RD. Therefore, we propose that rod loss triggers neurovascular changes that could affect cone survival. This discussion is driven by persisting questions about the mechanisms responsible for their inevitable death.

As illustrated in Figure 9A, arrow 1, a “death signal” from degenerating rod photoreceptors can trigger cone cell loss via a gap-junction–mediated “bystander” effect (14). The same mechanism has also been suggested in glaucoma-induced progressive loss of ganglion cells (38). Rods can also promote cone survival by releasing a viability paracrine factor; in the absence of rods, cones survival is diminished (15, 16). Rods also have reciprocal metabolic interactions with RPE cells (Figure 9A, arrow 2). Specifically, glucose from the choroidal blood is delivered by RPE cells to both rod and cone photoreceptors. More numerous rods burn the glucose, feeding lactate back to the RPE cells (39). It is possible that when this metabolic pathway is disrupted, i.e., during loss of rods in *rd10* mice, RPE cells will retain glucose, starving cone photoreceptors. This is supported by the finding that metabolic stress in RPE alone triggered glucose retention and photoreceptor cell death (Figure 9A, arrow 3; ref. 40). Tight junctions between RPE cells are also directly affected by the rods. In the *Nrl^{-/-}* retina where rods were genetically converted into cones, tight junctions of RPE and retinal vasculature became leaky (18). Consistent with these findings, our data demonstrate that tight junctions become leaky early in RD. Later on, lost interactions with photoreceptors could lead to further stress in RPE cells and their death, exposing choroid in the central retina (Figure 9B, right).

Other factors, such as recruitment of activated microglia can exacerbate degradation of cone photoreceptors (41). Our finding that, in the areas of compromised RPE, Müller glia became attracted to the choroid was intriguing (Figure 9A, arrow 4). We found that the presence of Müller cells was associated with aberrant expression of tight junction components in choroid, a non-CNS vascular system. Whereas it is unclear whether Müller glia contact choroid directly, a remote interaction between them, possibly through endosome secretion, might be sufficient to induce BRB changes (42). Activation of Müller glia and its accumulation at the sites of exposed choroid may serve to partially “seal” the leak by inducing atypical BRB properties in the otherwise leaky choroid (Figure 9B, right). Indeed, Müller glia have been shown to be both necessary and sufficient to induce blood barrier in fenestrated non-CNS blood vessels. Retinal conditional ablation of Müller cells led to disruption of BRB and vascular leak (43); *in vivo* injection of rabbit Müller cells into anterior chamber of the rat eye led to formation of the barrier in the iris (36).

Neurovascular interactions in RD. In patients, and in rodent models with overlapping incidence of RD and persistent hyperglycemia, the absence of rods precluded neovascularization caused by diabetic retinopathy (44, 45). Activation of rods during dark adaptation worsened diabetic retinopathy in human patients (46), while their suppression during exposure to light improved diabetic retinopathy outcomes (47). These findings reveal a key role for functional rods in the maintenance of the vascular network. Our work further demonstrates that following the loss of rods, and once the RPE-mediated outer BRB was compromised, the retina is exposed to blood components from fenestrated choroid (Figure 9A, arrow 5). Retinal edema, a major cause of vision loss in human patients with RD and AMD (19, 48–51), also prevalent in rodents (52) and primates (53), could be the result of this BRB breakdown. Our data suggest that cone survival could be compromised as the disruption of BRB becomes more severe. In both humans and mice, 95% of

all photoreceptors are rods (27, 54), contributing over 50% to retina thickness. This bulk of tissue serves not only as a natural barrier between choroid and retinal vasculature, but also is the major energy consumer in the retina. In the absence of rods and because choroidal blood vessels are not autoregulated by local oxygen levels (55–57), the excess of oxygen delivered by choroid may eliminate the need for retinal blood vessels in the deep vascular layer (Figure 9A, arrow 6). Although the mechanisms of this vascular “pruning” are yet to be determined, our findings are consistent with observations in a variety of RD models exhibiting deep vascular layer dystrophy (*rd1*, *rd10* mice, ref. 20; P23H mouse, ref. 58; P23H and S334ter rats, ref. 59). Similar events have also been implicated in more typical vascular diseases, such as diabetic retinopathy, where neurons were shown to induce aberrant vascular changes (60, 61).

In *rd10* mice, alterations of the vascular network and BRB integrity were observed at P35–P40 when most of rods were already lost. However, a reduced capillary blood flow determined in the current study and in other animal models of RD (20, 58) as well as in patients with *Retinitis pigmentosa* (62–65), resulting from a significant reduction in vascular diameter and the presence of nonperfused retinal blood vessels, indicates that the functional effect of disrupted rod signaling may occur much earlier. Diminished blood flow could thus exacerbate rod degeneration and diminish cone survival. Indeed, a treatment with systemic hyperoxia has been shown to slow the rate of photoreceptor death in animal models (66–68) and patients with *Retinitis pigmentosa* (69), suggesting that insufficient blood supply in early RD contributes to photoreceptor dysfunction.

Due to the inherent complexity of RD pathology, our ability to directly test the causal link between neuronal and vascular changes is limited. To distinguish among early changes in neuronal activity, neurovascular deficit, and cell loss, novel models exhibiting slower or inducible cell loss will be needed. For instance, disruption of the BRB has been studied in blood-injected and light damage–induced RD models (70, 71). We are currently evaluating whether changing severity of light stimuli would enable the separation of activity-dependent and neuronal loss–dependent vascular changes. In conclusion, we identified remodeling of the neurovascular unit, BRB breakdown, and vascular leaks early in the course of RD. Since these changes were accompanied by cone degeneration and declining cone vision, they suggest that correcting neurovascular pathology may provide a new approach for treating RD.

Methods

Animals. WT (C57BL/6J, RRID:IMSR_JAX:000664) and homozygous *rd10* (B6.CXB1-Pde6brd10/J, RRID:IMSR_JAX:004297) mice of both sexes were obtained from the Jackson Laboratory and used at P35–P40 and P180–200. All mice were on a regular 12-hour light/12-hour dark cycle.

Antibodies and other reagents. Antibodies used in this study were as follows: goat anti-mouse albumin (Bethyl, A90-234A, 1:800, RRID:AB_67122); rabbit anti-NG2 chondroitin sulfate proteoglycan, Cy3 conjugate (EMD MilliporeSigma, AB5320C3, 1:800, RRID:AB_11214368); mouse anti-claudin5 clone 4C3C2, Alexa Fluor 488 conjugate (Invitrogen, 352588, 1:10,000, RRID:AB_2532189); rat anti-PLVAP/MECA-32 (BD Biosciences, Pharmingen, 553849, 1:10,000, RRID:AB_395086); rabbit connexin 43 (MilliporeSigma, C6219, 1:2000, RRID:AB_476857); mouse anti-glutathione synthetase (MilliporeSigma, MAB302, 1:2000, RRID:AB_2110656); rabbit anti-cone arrestin (MilliporeSigma, AB15282, 1:10000, RRID:AB_1163387). *Griffonia simplicifolia* isolectins conjugated to a fluorescent label were from Invitrogen (GS-IB4 Alexa Fluor 488, I21411, RRID:AB_2314665; GS-IB4 Alexa Fluor 568, I21412). Isolectin stock solution was made using 500 µg isolectin powder dissolved in 500 µl PBS-calcium solution: 8.1 mM Na₂HPO₄ dibasic, 1.9 mM NaH₂PO₄ monobasic, 154 mM NaCl, 1 mM CaCl₂. Isolectin stock solution was diluted 1:400 and applied with the secondary antibodies. Phalloidin coupled to Alexa Fluor 488 (Biotium, 00042-T) was prepared by adding 250 µl water to 50 U of fluorescent phalloidin and was used in a final concentration of 1:400. Secondary antibodies were conjugated to Alexa Fluor 488 (1:1000; green fluorescence, Molecular Probes), Alexa Fluor 568 (1:1000; red fluorescence, Molecular Probes), Alexa Fluor 647 (1:400; far red fluorescence, Molecular probes), or Cy5 (1:500; far red fluorescence, Jackson ImmunoResearch).

Immunohistochemistry. After euthanasia, eyes were removed and placed in bicarbonate-buffered Ames' medium (MilliporeSigma) equilibrated with 95% O₂ and 5% CO₂. The cornea was removed by an encircling cut above ora serrata, and the iris, lens, and vitreous were extracted. The remaining eyecup, with the retina still attached to the pigment epithelium, was submersion-fixed on a shaker in freshly prepared 4% carbodiimide and 0.25% paraformaldehyde in 0.1 M PBS (pH = 7.3, for staining with PLVAP, Cx43, claudin-5) or 4% paraformaldehyde in PBS (all other staining) for 15 minutes at room temperature. After fixation, the eyecups were washed in PBS for 2 hours. Retinal eyecup preparations were blocked for 10

hours in a PBS solution containing 5% Chemiblocker (membrane-blocking agent, Chemicon), 0.5% Triton X-100, and 0.05% sodium azide (MilliporeSigma). Primary antibodies were diluted in the same solution and applied for 96 hours, followed by incubation for 48 hours in the appropriate secondary antibody. In multilabeling experiments, eyecup preparations were incubated in a mixture of primary antibodies, followed by a mixture of secondary antibodies. All steps were completed at room temperature. After staining, the tissue was flat mounted on a slide, ganglion cell layer up, and coverslipped using Vectashield mounting medium (H-1000, Vector Laboratories). The coverslip was sealed in place with nail polish. To avoid extensive squeezing and damage to the retina, small pieces of a broken glass cover slip (number 1 size) were placed in the space between the slide and the coverslip.

Fluorescent probes for in vivo and in vitro imaging. To measure BBB permeability, the following probe sizes were used: 0.376-kDa sodium fluorescein (NaF, 100 μ l of 1% solution i.v.), 3- to 5-kDa dextran-FITC (100 μ l of 1% solution i.v.), 10-kDa dextran-FITC (100 μ l of 1% solution i.v.), approximately 69-kDa Evans Blue/Albumin (EB; MW ~69 kDa after binding to plasma albumin; 100 μ l of 2% solution i.v.). Albumin was indirectly visualized after immunohistochemical staining for albumin.

In vivo imaging. Mice were anesthetized with a mixture of 150 mg/kg ketamine and 15 mg/kg xylazine. The pupils were dilated with 0.5% tropicamide ophthalmic solution, and a coverslip was placed on each eye with GONAK ophthalmic solution. Mice were mounted with SG-4N mouse head holder (Narishige) on an inverted Nikon Eclipse Ti-U confocal microscope. Fluorescent probes were injected into a tail vein, except for Evans Blue, which was injected i.p. Thirty minutes following the probe injection, the eyes were imaged with $\times 4$ and $\times 10$ long-distance air objectives. For blood flow analysis, video images at 120 frames per second were captured with a microscope-mounted Sony A7 s camera.

In vitro imaging. Probes were injected into a tail vein, and after 30 minutes the animal was euthanized and the eyes were removed and placed into bicarbonate-buffered Ames' medium equilibrated with 95% O₂ and 5% CO₂. The cornea was removed by the encircling cut below ora serrata. The iris, lens, and vitreous were removed. The remaining eyecup, with the retina still attached to the pigment epithelium, was cut to enable flat mounting. The eyecup preparation was attached to a PTFE Membrane Insert (72), transferred to a Nikon Eclipse Ti-U confocal microscope and imaged with a $\times 20$ objective.

Parallel in vivo, in vitro, and fixed tissue assessment. We evaluated inner and outer BRB integrity by developing a protocol that used established and potentially new BRB markers (Figure 1). The protocol also enabled transitions between in vivo, in vitro, and fixed tissue assessment as described previously (73). Thirty minutes prior to tissue collection, mice were i.p. injected with Evans Blue to identify perfusable blood vessels and vascular leak (Figure 1B). Next, eyecup preparations were made and retinal poles were identified (Figure 1C) based on the pattern of choroid landmarks as described previously (74). In immunolabeled retinal whole mounts, blood vessels were distinguished based on the morphological properties and expression of smooth muscle actin (SMA, Figure 1D). Arteries were positive for SMA; veins had larger diameter and were directly fed by capillaries. Order of the capillaries was established by counting the branching points from the major artery. The Evans Blue-labeled eyecups were imaged and processed for staining with structural (isolectin) and functional (albumin, NG2) markers and assessed again in the same areas (Figure 1, E–G). In the fixed tissue, the albumin marker overlapped with the Evans Blue labeling in vitro; both markers identified perfusable blood vessels (Figure 1, E–G, arrow in *rd10*); in addition, in *rd10* retina, leaky capillaries were defined by fluorescence outside the blood vessels (Figure 1G, arrowheads). The pericytes resided around living blood vessels. Isolectin labeled the basement membrane of living and deteriorating (nonperfusable) blood vessels (Figure 1F). We confirmed this by labeling against NG2-positive pericytes and CD31-positive endothelial cells (Figure 1, H and I). In WT mice, isolectin labeled basement membrane around bridging pericytes in the absence of endothelial cells (Figure 1H). In *rd10* mice, it also labeled deteriorating blood vessels lacking both endothelial cells and pericytes (Figure 1I).

Quantification of retinal vasculature and cone survival. All data were analyzed in ImageJ (NIH) (<http://imagej.nih.gov/ij/>, RRID: SCR_003070). Arteries were distinguished from veins by smaller diameter and by a capillary-free zone around them. Identification was confirmed by immunostaining for SMA. Z-stacks from living and fixed eye preparations were imaged with a $\times 20$ objective (Nikon). To quantify the intensity and location of the leak, a confocal Z-stack through the entire thickness of the retina, including RPE cells, was taken. Within each layer (superficial, intermediate, deep, and RPE) of the same Z-stack, an approximately 6- μ m-thick projection was made (typically 2–3 confocal sections). In those individual projections, the median fluorescence intensity in the areas outside the blood vessels and at the level of RPE was normalized to the median intensity within the blood vessels (Figure 2E) and the ratio was plotted as a fluorescence profile of

the retina. In this fluorescent profile, the layer with the maximal fluorescence intensity was considered to be the source of the leak. Density of the functional blood vessels was established in albumin-labeled retina by thresholding images and applying skeletonizing procedure in ImageJ. Pericytes were manually counted in the capillaries of NG2-labeled retinas. For correlation between cone loss and the magnitude of the vascular leak, an entire eyecup preparation was scanned with a $\times 4$ objective (Nikon) and analyzed in a photomerge. Both vascular leak and cone images were thresholded and quantified as a fraction of the area above the threshold. Central retina was defined as the area from the optic nerve to half radius in all directions.

Virtual optokinetic system. A virtual optokinetic system (ref. 75) was used to measure visual spatial frequency thresholds. Four computer monitors facing inward created the walls of a square testing arena. A virtual cylinder, covered with of a vertical sine-wave grating, was drawn and projected onto the monitors using software (OptoMotry; <http://www.cerebralmechanics.com/>). A mouse was placed on a platform at the epicenter of the arena, and a video camera, situated above the animal, provided real-time video feedback on an external computer monitor (Figure 2A). Mice were allowed to move freely on the platform, and an experimenter manually tracked their forehead position in real time to maintain the hub of the cylinder at the animal's viewing position. Visual thresholds were obtained with a staircase procedure in which the step size was halved after each reversal and was terminated when the step size became smaller than the hardware resolution (0.003 cycles/degree). The maximum spatial frequency capable of driving optokinetic tracking was determined and termed a spatial frequency threshold. Typically, an animal's testing session (thresholds in 2 directions) lasted 10–20 minutes. One staircase was completed for each direction of rotation of the stimulus, which isolates the function of each eye (76), with the 2 staircases being randomly interleaved.

Experimental design. Data exclusion rules were as follows: data from a given animal were not excluded unless health problems or abnormalities, such as microcephaly, eye injury, or other unintended genetic variations called collected data into question. For a given day's experiment, animal genotype and age group were chosen at random. When experimentally feasible, animal selection, euthanasia, and retinal preparation were done by someone other than the person doing the experiment. The data are presented as mean \pm SEM, unless otherwise indicated. The number of samples (n) indicates number of animals per group. Due to inherent biological variability in live animals and donor tissue, all numbers represent a biological replication (same test on multiple samples or distinct regions of the same sample), rather than technical replication (same test on same sample). To avoid introduction of nonindependent data into statistical analysis, first, multiple samples from individual animals were averaged within subject, and then, the data between animals were compared (77).

Statistics. Statistical analysis was performed in either SPSS v.19 (IBM, RRID:SCR_003210) or SigmaPlot v.11 (Systat, RRID:SCR_003210), using 2-tailed t test. A P value less than 0.05 was considered significant. For multiple comparisons, ANOVA with post-hoc Tukey's test or repeated-measures ANOVA was used. To compute an appropriate sample size, a priori power analyses were performed with target error values α and β both = 0.05 (power = 0.95) and ANOVA effect size $f = 0.4$. Data collection for a particular experiment stopped if a minimum sample size of $n = 4$ animals was met for all experimental groups and the calculated P value for the measurements specific to the given experiment reached significance $P < 0.0001$.

Study approval. This study was performed in strict accordance with the recommendations in the *Guide for the Care and Use of Laboratory Animals* (National Academies Press, 2011). All of the animals were handled according to approved institutional animal care and use committee (IACUC) protocols (0809-785) of Weill Cornell Medicine. All procedures in live animals were performed under IACUC-approved anesthesia, and every effort was made to minimize suffering.

Author contributions

EI, NMA, GTP, and BTS designed all aspects of research studies, conducted experiments, acquired and analyzed data, and wrote the manuscript.

Acknowledgments

This work was supported by NIH grants NIH grants R01-EY026576 and R01-EY029796 (to BTS). The authors thank Rajiv Ratan for comments on the manuscript.

Address correspondence to: Botir T. Sagdullaev or Elena Ivanova, 785 Mamaroneck Avenue, White Plains, New York 10605, USA. Phone: 914.368.3167; Email: bos2005@med.cornell.edu (BTS). Phone: 914.368.3168; Email: eli3001@med.cornell.edu (EI).

1. Iadecola C. The pathobiology of vascular dementia. *Neuron*. 2013;80(4):844–866.
2. Montagne A, et al. Blood-brain barrier breakdown in the aging human hippocampus. *Neuron*. 2015;85(2):296–302.
3. Zhong Z, et al. ALS-causing SOD1 mutants generate vascular changes prior to motor neuron degeneration. *Nat Neurosci*. 2008;11(4):420–422.
4. Zille M, et al. Neuronal Death After Hemorrhagic Stroke In Vitro and In Vivo Shares Features of Ferroptosis and Necroptosis. *Stroke*. 2017;48(4):1033–1043.
5. Zlokovic BV. Neurovascular pathways to neurodegeneration in Alzheimer's disease and other disorders. *Nat Rev Neurosci*. 2011;12(12):723–738.
6. Sweeney MD, Sagare AP, Zlokovic BV. Blood-brain barrier breakdown in Alzheimer disease and other neurodegenerative disorders. *Nat Rev Neurol*. 2018;14(3):133–150.
7. Campbell M, Humphries P. The blood-retina barrier: tight junctions and barrier modulation. *Adv Exp Med Biol*. 2012;763:70–84.
8. Ferrari S, Di Iorio E, Barbaro V, Ponzin D, Sorrentino FS, Parmeggiani F. Retinitis pigmentosa: genes and disease mechanisms. *Curr Genomics*. 2011;12(4):238–249.
9. Gargini C, Terzibasi E, Mazzoni F, Strettoi E. Retinal organization in the retinal degeneration 10 (rd10) mutant mouse: a morphological and ERG study. *J Comp Neurol*. 2007;500(2):222–238.
10. Swaroop A, Kim D, Forrest D. Transcriptional regulation of photoreceptor development and homeostasis in the mammalian retina. *Nat Rev Neurosci*. 2010;11(8):563–576.
11. Murakami Y, et al. Necrotic cone photoreceptor cell death in retinitis pigmentosa. *Cell Death Dis*. 2015;6:e2038.
12. Narayan DS, Wood JP, Chidlow G, Casson RJ. A review of the mechanisms of cone degeneration in retinitis pigmentosa. *Acta Ophthalmol*. 2016;94(8):748–754.
13. Punzo C, Kornacker K, Cepko CL. Stimulation of the insulin/mTOR pathway delays cone death in a mouse model of retinitis pigmentosa. *Nat Neurosci*. 2009;12(1):44–52.
14. Ripps H. Cell death in retinitis pigmentosa: gap junctions and the 'bystander' effect. *Exp Eye Res*. 2002;74(3):327–336.
15. Léveillard T, et al. Identification and characterization of rod-derived cone viability factor. *Nat Genet*. 2004;36(7):755–759.
16. Mohand-Said S, et al. Normal retina releases a diffusible factor stimulating cone survival in the retinal degeneration mouse. *Proc Natl Acad Sci USA*. 1998;95(14):8357–8362.
17. Joyal JS, et al. Retinal lipid and glucose metabolism dictates angiogenesis through the lipid sensor Ffar1. *Nat Med*. 2016;22(4):439–445.
18. Roger JE, et al. Preservation of cone photoreceptors after a rapid yet transient degeneration and remodeling in cone-only Nrl^{-/-} mouse retina. *J Neurosci*. 2012;32(2):528–541.
19. Adackapara CA, Sunness JS, Dibernardo CW, Melia BM, Dagnelie G. Prevalence of cystoid macular edema and stability in ocular retinal thickness in eyes with retinitis pigmentosa during a 48-week lutein trial. *Retina (Philadelphia, Pa)*. 2008;28(1):103–110.
20. Otani A, et al. Rescue of retinal degeneration by intravitreally injected adult bone marrow-derived lineage-negative hematopoietic stem cells. *J Clin Invest*. 2004;114(6):765–774.
21. Alam NM, Altimus CM, Douglas RM, Hattar S, Prusky GT. Photoreceptor regulation of spatial visual behavior. *Invest Ophthalmol Vis Sci*. 2015;56(3):1842–1849.
22. Chang B, Hawes NL, Hurd RE, Davisson MT, Nusinowitz S, Heckenlively JR. Retinal degeneration mutants in the mouse. *Vision Res*. 2002;42(4):517–525.
23. Ecker JL, et al. Melanopsin-expressing retinal ganglion-cell photoreceptors: cellular diversity and role in pattern vision. *Neuron*. 2010;67(1):49–60.
24. Savinova OV, et al. Intraocular pressure in genetically distinct mice: an update and strain survey. *BMC Genet*. 2001;2:12.
25. Ivanova E, Kovacs-Oller T, Sagdullaev BT. Vascular Pericyte Impairment and Connexin43 Gap Junction Deficit Contribute to Vasomotor Decline in Diabetic Retinopathy. *J Neurosci*. 2017;37(32):7580–7594.
26. Artal P, Herreros de Tejada P, Muñoz Tedó C, Green DG. Retinal image quality in the rodent eye. *Vis Neurosci*. 1998;15(4):597–605.
27. Jeon CJ, Strettoi E, Masland RH. The major cell populations of the mouse retina. *J Neurosci*. 1998;18(21):8936–8946.
28. Stan RV, Kubitza M, Palade GE. PV-1 is a component of the fenestral and stomatal diaphragms in fenestrated endothelia. *Proc Natl Acad Sci USA*. 1999;96(23):13203–13207.
29. Beltramo E, Porta M. Pericyte loss in diabetic retinopathy: mechanisms and consequences. *Curr Med Chem*. 2013;20(26):3218–3225.
30. Hammes HP, et al. Pericytes and the pathogenesis of diabetic retinopathy. *Diabetes*. 2002;51(10):3107–3112.
31. Armulik A, et al. Pericytes regulate the blood-brain barrier. *Nature*. 2010;468(7323):557–561.
32. Nitta T, et al. Size-selective loosening of the blood-brain barrier in claudin-5-deficient mice. *J Cell Biol*. 2003;161(3):653–660.
33. Jaissle GB, et al. Bone spicule pigment formation in retinitis pigmentosa: insights from a mouse model. *Graefes Arch Clin Exp Ophthalmol*. 2010;248(8):1063–1070.
34. Milam AH, et al. Concentric retinitis pigmentosa: clinicopathologic correlations. *Exp Eye Res*. 2001;73(4):493–508.
35. Edwards MM, McLeod DS, Bhutto IA, Grebe R, Duffy M, Luty GA. Subretinal Glial Membranes in Eyes With Geographic Atrophy. *Invest Ophthalmol Vis Sci*. 2017;58(3):1352–1367.
36. Tout S, Chan-Ling T, Holländer H, Stone J. The role of Müller cells in the formation of the blood-retinal barrier. *Neuroscience*. 1993;55(1):291–301.
37. Holopigian K, Seiple W, Greenstein VC, Hood DC, Carr RE. Local cone and rod system function in patients with retinitis pigmentosa. *Invest Ophthalmol Vis Sci*. 2001;42(3):779–788.
38. Akopian A, et al. Gap junction-mediated death of retinal neurons is connexin and insult specific: a potential target for neuroprotection. *J Neurosci*. 2014;34(32):10582–10591.
39. Kanow MA, et al. Biochemical adaptations of the retina and retinal pigment epithelium support a metabolic ecosystem in the vertebrate eye. *Elife*. 2017;6:e28899.
40. Kurihara T, et al. Hypoxia-induced metabolic stress in retinal pigment epithelial cells is sufficient to induce photoreceptor degeneration. *Elife*. 2016;5:e14319.
41. Gupta N, Brown KE, Milam AH. Activated microglia in human retinitis pigmentosa, late-onset retinal degeneration, and age-related macular degeneration. *Exp Eye Res*. 2003;76(4):463–471.

42. Zhao Z, Zlokovic BV. Remote control of BBB: A tale of exosomes and microRNA. *Cell Res.* 2017;27(7):849–850.
43. Shen W, et al. Conditional Müllercell ablation causes independent neuronal and vascular pathologies in a novel transgenic model. *J Neurosci.* 2012;32(45):15715–15727.
44. Arden GB. The absence of diabetic retinopathy in patients with retinitis pigmentosa: implications for pathophysiology and possible treatment. *Br J Ophthalmol.* 2001;85(3):366–370.
45. de Gooyer TE, Stevenson KA, Humphries P, Simpson DA, Gardiner TA, Stitt AW. Retinopathy is reduced during experimental diabetes in a mouse model of outer retinal degeneration. *Invest Ophthalmol Vis Sci.* 2006;47(12):5561–5568.
46. Arden GB, Wolf JE, Tsang Y. Does dark adaptation exacerbate diabetic retinopathy? Evidence and a linking hypothesis. *Vision Res.* 1998;38(11):1723–1729.
47. Arden GB, Jyothi S, Hogg CH, Lee YF, Sivaprasad S. Regression of early diabetic macular oedema is associated with prevention of dark adaptation. *Eye (Lond).* 2011;25(12):1546–1554.
48. Fishman GA, Fishman M, Maggiano J. Macular lesions associated with retinitis pigmentosa. *Arch Ophthalmol.* 1977;95(5):798–803.
49. Hajali M, Fishman GA, Anderson RJ. The prevalence of cystoid macular oedema in retinitis pigmentosa patients determined by optical coherence tomography. *Br J Ophthalmol.* 2008;92(8):1065–1068.
50. Liew G, Moore AT, Bradley PD, Webster AR, Michaelides M. Factors associated with visual acuity in patients with cystoid macular oedema and Retinitis Pigmentosa. *Ophthalmic Epidemiol.* 2018;25(3):183–186.
51. Sandberg MA, Brockhurst RJ, Gaudio AR, Berson EL. The association between visual acuity and central retinal thickness in retinitis pigmentosa. *Invest Ophthalmol Vis Sci.* 2005;46(9):3349–3354.
52. Wang Q, et al. Photoreceptor degeneration changes magnetic resonance imaging features in a mouse model of retinitis pigmentosa. *Magn Reson Med.* 2011;65(6):1793–1798.
53. Ikeda Y, et al. Discovery of a Cynomolgus Monkey Family With Retinitis Pigmentosa. *Invest Ophthalmol Vis Sci.* 2018;59(2):826–830.
54. Curcio CA, Sloan KR, Kalina RE, Hendrickson AE. Human photoreceptor topography. *J Comp Neurol.* 1990;292(4):497–523.
55. Alm A, Bill A. The oxygen supply to the retina. I. Effects of changes in intraocular and arterial blood pressures, and in arterial P_O2 and P_{CO}2 on the oxygen tension in the vitreous body of the cat. *Acta Physiol Scand.* 1972;84(2):261–274.
56. Flower RW, Fryczkowski AW, McLeod DS. Variability in choriocapillaris blood flow distribution. *Invest Ophthalmol Vis Sci.* 1995;36(7):1247–1258.
57. Riva CE, Cranstoun SD, Mann RM, Barnes GE. Local choroidal blood flow in the cat by laser Doppler flowmetry. *Invest Ophthalmol Vis Sci.* 1994;35(2):608–618.
58. Liu H, et al. Photoreceptor Cells Influence Retinal Vascular Degeneration in Mouse Models of Retinal Degeneration and Diabetes. *Invest Ophthalmol Vis Sci.* 2016;57(10):4272–4281.
59. Pennesi ME, Nishikawa S, Matthes MT, Yasumura D, LaVail MM. The relationship of photoreceptor degeneration to retinal vascular development and loss in mutant rhodopsin transgenic and RCS rats. *Exp Eye Res.* 2008;87(6):561–570.
60. Arden GB, Sidman RL, Arap W, Schlingemann RO. Spare the rod and spoil the eye. *Br J Ophthalmol.* 2005;89(6):764–769.
61. Kern TS. Do photoreceptor cells cause the development of retinal vascular disease? *Vision Res.* 2017;139:65–71.
62. Grunwald JE, Maguire AM, Dupont J. Retinal hemodynamics in retinitis pigmentosa. *Am J Ophthalmol.* 1996;122(4):502–508.
63. Ma Y, et al. Quantitative analysis of retinal vessel attenuation in eyes with retinitis pigmentosa. *Invest Ophthalmol Vis Sci.* 2012;53(7):4306–4314.
64. Nakagawa S, Oishi A, Ogino K, Makiyama Y, Kurimoto M, Yoshimura N. Association of retinal vessel attenuation with visual function in eyes with retinitis pigmentosa. *Clin Ophthalmol.* 2014;8:1487–1493.
65. Wolf S, Pöstgens H, Bertram B, Schulte K, Teping C, Reim M. [Hemodynamic findings in patients with retinitis pigmentosa]. *Klin Monbl Augenheilkd.* 1991;199(5):325–329.
66. Choi MY, Yu YS, Kim SK, Kim YJ, Seo JS. The effect of oxygen on retinal degeneration in wild-type and hsp70.1 knockout neonatal retinal degeneration mice. *Korean J Ophthalmol.* 2001;15(1):1–7.
67. Maslim J, Valter K, Egensperger R, Holländer H, Stone J. Tissue oxygen during a critical developmental period controls the death and survival of photoreceptors. *Invest Ophthalmol Vis Sci.* 1997;38(9):1667–1677.
68. Valter K, Maslim J, Bowers F, Stone J. Photoreceptor dystrophy in the RCS rat: roles of oxygen, debris, and bFGF. *Invest Ophthalmol Vis Sci.* 1998;39(12):2427–2442.
69. Vingolo EM, Rocco M, Grenga P, Salvatore S, Pelaia P. Slowing the degenerative process, long lasting effect of hyperbaric oxygen therapy in retinitis pigmentosa. *Graefes Arch Clin Exp Ophthalmol.* 2008;246(1):93–98.
70. Zhao L, Ma W, Fariss RN, Wong WT. Minocycline attenuates photoreceptor degeneration in a mouse model of subretinal hemorrhage microglial: inhibition as a potential therapeutic strategy. *Am J Pathol.* 2011;179(3):1265–1277.
71. Geiger P, Barben M, Grimm C, Samardzija M. Blue light-induced retinal lesions, intraretinal vascular leakage and edema formation in the all-cone mouse retina. *Cell Death Dis.* 2015;6:e1985.
72. Ivanova E, Toychiev AH, Yee CW, Sagdullaev BT. Optimized protocol for retinal wholemount preparation for imaging and immunohistochemistry. *J Vis Exp.* 2013;(82):e51018.
73. Toychiev AH, Ivanova E, Yee CW, Sagdullaev BT. Block of gap junctions eliminates aberrant activity and restores light responses during retinal degeneration. *J Neurosci.* 2013;33(35):13972–13977.
74. Wei W, Elstrott J, Feller MB. Two-photon targeted recording of GFP-expressing neurons for light responses and live-cell imaging in the mouse retina. *Nat Protoc.* 2010;5(7):1347–1352.
75. Prusky GT, Alam NM, Beekman S, Douglas RM. Rapid quantification of adult and developing mouse spatial vision using a virtual optomotor system. *Invest Ophthalmol Vis Sci.* 2004;45(12):4611–4616.
76. Douglas RM, Alam NM, Silver BD, McGill TJ, Tschetter WW, Prusky GT. Independent visual threshold measurements in the two eyes of freely moving rats and mice using a virtual-reality optokinetic system. *Vis Neurosci.* 2005;22(5):677–684.
77. Aarts E, Verhage M, Veenvliet JV, Dolan CV, van der Sluis S. A solution to dependency: using multilevel analysis to accommodate nested data. *Nat Neurosci.* 2014;17(4):491–496.